

A Robust Dual-Frequency Radar Profiling Algorithm

MIRCEA GRECU AND LIN TIAN

*Goddard Earth Sciences and Technology Center, University of Maryland Baltimore County, Baltimore,
and Laboratory for Atmospheres, NASA Goddard Space Flight Center, Greenbelt, Maryland*

WILLIAM S. OLSON

*Joint Center for Earth Systems Technology, University of Maryland Baltimore County, Baltimore,
and Laboratory for Atmospheres, NASA Goddard Space Flight Center, Greenbelt, Maryland*

SIMONE TANELLI

Jet Propulsion Laboratory, California Institute of Technology, Pasadena, California

(Manuscript received 16 September 2010, in final form 1 February 2011)

ABSTRACT

In this study, an algorithm to retrieve precipitation from spaceborne dual-frequency (13.8 and 35.6 GHz, or Ku/Ka band) radar observations is formulated and investigated. Such algorithms will be of paramount importance in deriving radar-based and combined radar–radiometer precipitation estimates from observations provided by the forthcoming NASA Global Precipitation Measurement (GPM) mission. In GPM, dual-frequency Ku-/Ka-band radar observations will be available only within a narrow swath (approximately one-half of the width of the Ku-band radar swath) over the earth's surface. Therefore, a particular challenge is to develop a flexible radar retrieval algorithm that can be used to derive physically consistent precipitation profile estimates across the radar swath irrespective of the availability of Ka-band radar observations at any specific location inside that swath, in other words, an algorithm capable of exploiting the information provided by dual-frequency measurements but robust in the absence of Ka-band channel. In the present study, a unified, robust precipitation retrieval algorithm able to interpret either Ku-only or dual-frequency Ku-/Ka-band radar observations in a manner consistent with the information content of the observations is formulated. The formulation is based on 1) a *generalized* Hitschfeld–Bordan attenuation correction method that yields generic Ku-only precipitation profile estimates and 2) an optimization procedure that adjusts the Ku-band estimates to be physically consistent with coincident Ka-band reflectivity observations and surface reference technique–based path-integrated attenuation estimates at both Ku and Ka bands. The algorithm is investigated using synthetic and actual airborne radar observations collected in the NASA Tropical Composition, Cloud, and Climate Coupling (TC4) campaign. In the synthetic data investigation, the dual-frequency algorithm performed significantly better than a single-frequency algorithm; dual-frequency estimates, however, are still sensitive to various assumptions such as the particle size distribution shape, vertical and cloud water distributions, and scattering properties of the ice-phase precipitation.

1. Introduction

Knowledge regarding the three-dimensional variability of precipitation is essential in the development of precipitation retrieval algorithms from satellite radiometer observations. This is because satellite radiometer observations cannot be uniquely associated with precipitation,

and statistical information is required to determine optimal precipitation estimates. Spaceborne radar observations may be used to derive such information. For example, it is anticipated that in the Global Precipitation Measurement (GPM) era, observations from spaceborne dual-frequency radar will be used to develop algorithms capable of providing consistent precipitation estimates from satellite radiometers featuring various channel frequencies and footprint resolutions (Hou et al. 2008). Consistency among precipitation retrievals from these various radiometers will be achieved through

Corresponding author address: Dr. Mircea Grecu, Code 613.1, NASA/GSFC, 8800 Greenbelt Rd., Greenbelt, MD 20771.
E-mail: mircea.grecu-1@nasa.gov

the development of common precipitation–radiance databases derived from combined radar–radiometer precipitation profile estimates (Hou et al. 2008). From this perspective, spaceborne radar profiling algorithms are crucial for the derivation of global satellite precipitation estimates.

Various algorithms for retrieving precipitation from dual-frequency radar observations have been developed. These include, but are not limited to, methods by Meneghini et al. (1992), Mardiana et al. (2004), Grecu and Anagnostou (2004), Liao et al. (2005), and Rose and Chandrasekar (2006). In addition, methodologies for incorporating Ku-band radar observations in combined radar–radiometer retrieval frameworks have been formulated, for example, in Haddad et al. (1997), Grecu et al. (2004), and Masunaga and Kummerow (2005). However, further research must be conducted to develop dual-frequency retrieval algorithms that would perform optimally within the GPM context. The GPM core satellite will feature a Ku/Ka-band dual-frequency precipitation radar (DPR) (Senbokuya et al. 2004). The dual-frequency radar observations will be available within a 125-km-wide swath, centered within a 245-km-wide swath of single-frequency Ku-band radar observations. From the science perspective, it is desirable to develop a physically consistent radar profiling algorithm that can operate using either single-frequency (Ku band only) or dual-frequency (Ku/Ka band) observations, and one that can make use of path-integrated attenuation (PIA) estimates from the radar surface reference technique (SRT) (Meneghini et al. 2000, 2004) when deemed reliable.

In this study, we formulate a GPM DPR profiling algorithm that can be applied to both the inner and outer swaths and can optimally incorporate SRT information into the retrievals. The algorithm is based on a *generalized* Hitschfeld and Bordan (1954) attenuation correction methodology that yields generic Ku-band radar precipitation profile estimates and an optimization procedure that adjusts the Ku-band estimates to be physically consistent with coincident Ka-band observations and Ku/Ka-band SRT PIA estimates. The algorithm is computationally efficient and can be used within a combined radar–radiometer framework.

2. Method

a. Overview

The dual-frequency profiling algorithm formulated in this study is based on a computationally efficient methodology to derive generic precipitation profiles from single-frequency Ku-band radar observations. Specifically,

assuming that the hydrometeor particle size distributions follow a gamma function (Ulbrich 1983)—that is, $N(D) = N_0 D^\mu \exp(-\Lambda D)$, where D is the particle diameter and N_0 , Λ , and μ are the intercept, slope, and shape parameters, respectively—and that N_0 and μ along with the cloud water and water vapor attenuation are known for every gate, a Ku-band reflectivity profile is inverted to derive profiles of Λ . Various studies (e.g., Testud et al. 2001; Illingworth and Blackman 2002) showed that normalized gamma distributions are preferable to standard gamma distributions in some instances. However, because the number concentration still depends on the shape factor irrespective of whether a normalization is used (Liao et al. 2005), a standard gamma distribution is used in this study. To perform the dual-wavelength inversion, the Λ profiles are optimized as a function of adjustable N_0 profiles to minimize, in a least squares sense, the differences between Ka-band predicted and actual reflectivity observations, as well as the differences between predicted and SRT-derived Ku- and Ka-band PIAs. Additional constraint (background) terms are included in the function to be minimized to prevent the derivation of unrealistic N_0 values.

b. Single-frequency retrieval

A computationally efficient methodology to derive generic solutions from Ku-band observations was formulated by Hitschfeld and Bordan (1954, hereinafter HB). The traditional HB approach requires a power-law relationship between specific attenuation and reflectivity; that is,

$$k = \alpha Z^\beta, \quad (1)$$

where k is the specific attenuation, Z is the reflectivity factor, and α and β are known parameters. In addition to the power-law dependence, β has to be constant with range for the HB methodology to apply. A generalization of the HB method can be derived from the radar equation,

$$Z_m(r) = Z(r) \exp\left\{-0.2 \ln 10 \int_0^r k[Z(s)] ds\right\}, \quad (2)$$

where r is the radar range; $Z_m(r)$ and $Z(r)$ are the measured and unattenuated reflectivity factors, respectively; and $k[Z(s)]$ (dB km^{-1}) is the specific attenuation as a function of $Z(s)$. By raising (2) to power of β and then multiplying the result by $k[Z(r)]$, the following equation can be derived:

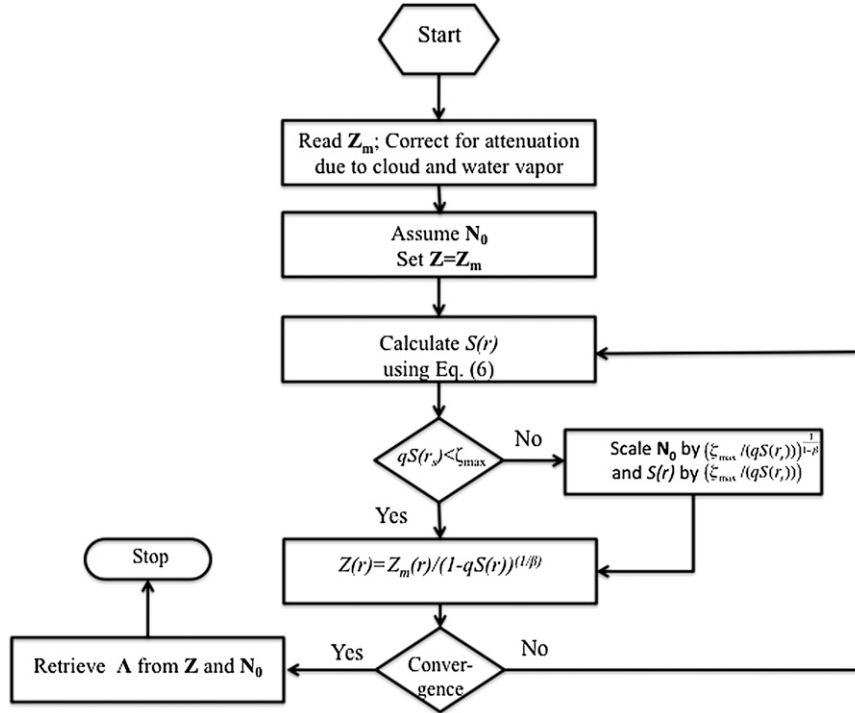


FIG. 1. Flowchart of the generalized Hitschfeld–Bordan procedure.

$$Z_m^\beta(r) \frac{k[Z(r)]}{Z^\beta(r)} = k[Z(r)] \exp \left\{ -0.2\beta \ln 10 \int_0^r k[Z(s)] ds \right\}. \quad (3)$$

where $q \equiv 0.2\beta \ln 10$. From (6), (7), and (2), it follows that the unattenuated reflectivity is related to the measured reflectivity by

$$Z(r) = Z_m(r) / [1 - qS(r)]^{1/\beta}. \quad (8)$$

The integration of (3) from 0 to r yields

$$\begin{aligned} 0.2\beta \ln 10 \int_0^r Z_m^\beta(s) \frac{k[Z(s)]}{Z^\beta(s)} ds \\ = 1 - \exp \left\{ -0.2\beta \ln 10 \int_0^r k[Z(s)] ds \right\}, \quad \text{or} \end{aligned} \quad (4)$$

$$\text{PIA}(r) = -10/\beta \log_{10} \left\{ 1 - 0.2\beta \ln 10 \int_0^r Z_m^\beta(s) \frac{k[Z(s)]}{Z^\beta(s)} ds \right\}, \quad (5)$$

where PIA is the two-way path-integrated attenuation. By defining

$$S(r) = \int_0^r Z_m^\beta(s) \frac{k[Z(s)]}{Z^\beta(s)} ds, \quad (6)$$

(5) can be rewritten

$$\text{PIA}(r) = -10/\beta \log_{10} [1 - qS(r)], \quad (7)$$

Equation (8), together with (6), is a generalization of the attenuation correction formula derived by HB. It is apparent from (6) and (8) that k does not have to satisfy (1) for the attenuation correction procedure to work. However, parameter β has to be constant in range and for numerical convergence considerations is chosen to minimize the variance of k/Z^β . However, if (1) holds, then the unattenuated reflectivity values do not need to be known to derive the PIA using (7) and (8). If (1) does not hold, an iterative solution is generally required. Shown in Fig. 1 is a flowchart describing an iterative attenuation correction procedure based on (6) and (8). The procedure starts by reading the observed reflectivity factors Z_m . Because (6) accounts only for attenuation due to solid, liquid, and mixed-phase precipitation, the measured reflectivity factors first need to be corrected for attenuation due to cloud and water vapor. This is done using parameterizations derived from cloud-resolving model simulations, as in Iguchi et al. (2009). Then, the initial estimates of the unattenuated reflectivity factors Z are set to Z_m . Because (8) does not have a closed

form (i.e., \mathbf{Z} occurs on both sides of the equation), iterative improvement of the approximations of \mathbf{Z} on the right-hand side of (8) is required.

The next step consists of calculating $S(r)$ for r varying from 0 (radar altitude) to r_s (range to the surface). When the quantity $qS(r_s)$ is greater than or equal to 1, (8) cannot be applied. Iguchi and Meneghini (1994) proposed the adjustment of $qS(r_s)$ by a factor ε , while Durden and Haddad (1998) and Ferreira et al. (2001) showed the importance of relating this type of adjustment to changes in the assumptions regarding the particle size distributions. Indeed, if the intercepts in the particle size distributions at all levels are changed by δN , then $qS(r_s)$ (where r_s is the range to the surface) changes $\delta N^{(1-\beta)}$, which implies that $\delta N^{(1-\beta)} = \varepsilon$. A simple procedure is implemented to keep the quantity $qS(r_s)$ below a maximum value ζ_{\max} (slightly less than 1) that corresponds to a maximum retrievable PIA value of $-10/\beta \log_{10}(1 - q\zeta_{\max})$. That is, if $qS(r_s)$ becomes greater than ζ_{\max} , it is set to ζ_{\max} and all particle size distribution (PSD) intercepts are changed by a factor of $\{\zeta_{\max}/[qS(r_s)]\}^{1/(1-\beta)}$. The unattenuated reflectivity factors can then be updated using (8).

The iterative procedure is continued until the root-mean-square difference between the updated and previous reflectivity factors does not change by more than 5×10^{-2} dB. Convergence is generally faster than that of the correction procedure of Meneghini (1978). This is because $k(Z)/Z^\beta$ is a weak function of Z (which may be a constant for certain ranges and drop size distributions, as assumed by HB). Moreover, (7) and (8) provide an effective and physically consistent mechanism of avoiding divergence in the attenuation correction process.

c. Lookup tables and forward model

To efficiently make use of the generality of formulas (6) and (8), lookup tables of attenuation and associated reflectivity, equivalent precipitation water content, and precipitation rate normalized by N_0 are derived as a function of Λ for constant μ at both Ku and Ka bands. Since these bulk radiative properties are normalized by N_0 , properties for different values of N_0 can be easily derived through simple calculations done on the fly. For example, if the attenuation for a given Ku-band reflectivity is desired, a quick search can be used to locate the two consecutive Z/N_0 entries in the lookup table that bound the actual Z/N_0 . The associated Ku-band k/N_0 value is determined through linear interpolation between the corresponding two consecutive k/N_0 values in the lookup table. Finally, k is determined by multiplying the interpolated k/N_0 by the actual N_0 value. A bisection method (Press et al. 2007) is used to quickly find the desired entries in the lookup tables.

Five values of μ are considered, that is, $\mu \in \{-2, -1, 0, 1, 2\}$. The values of Λ are chosen such that the mass-weighted mean diameter, defined as the ratio of the fourth moment of the gamma distribution to the third moment, varies from 0.1 to 5.0 mm with a step of 0.1 mm. That is, given a value of μ in the above set and a value of mean diameter, Λ is analytically determined and the normalized reflectivity and attenuation are determined by numerical integration. Multiple hydrometeor phases are considered as well. For stratiform rain exhibiting a clear bright band, the five-node storm structure of Iguchi et al. (2009) is used. That is, the bright band (if it exists) is first identified and used to define the geometry of the melting layer. Then, depending on the altitude of a given range gate relative to the melting layer boundaries, specific lookup tables are used for attenuation correction and PSD estimation. Within the melting layer itself, a brightband model similar to the first model of Bauer et al. (2000) is used to derive the attenuation and reflectivity. That is, snow is assumed to have a constant density at the top of the melting layer and the precipitation flux is assumed to be constant within the melting layer. The first model of Bauer et al. (2000) is integrated downward to derive the amount of melted mass as a function of the distance below the 0.0°C isotherm. The electromagnetic properties of melting snow are calculated using the model proposed by Klaassen (1988). The attenuation, reflectivity, and associated precipitation table for the brightband peak (node C) is constructed by matching the peak reflectivity in the computational melting layer model. A snow lookup table is used at the top of the melting layer (node B). Snow particles are modeled as a spherical mixture of air and ice in this study. The Maxwell-Garnett formula (Maxwell-Garnett 1904) is used to determine the snow refractive index. A water lookup table is used at the bottom of the melting layer (node D). Nodes B and D are set at 500 m above and below the brightband peak. Tables for the top and bottom nodes (A and E) are derived using snow and water properties at temperatures estimated as a function of the distance from the bright band, assuming a 6 K km⁻¹ lapse rate. The attenuation versus reflectivity relationships in between these nodes are determined through linear interpolation. It should be mentioned that the lapse rate can also be determined using meteorological analyses. Moreover, nodes B and D might be more accurately determined based on the reflectivity derivative with range. A similar methodology, but based only on four nodes, is used in stratiform rain not exhibiting a bright band and in convective rain. That is, node C is eliminated and the attenuation versus reflectivity relationships within the transition are determined by interpolating between the node B and node D tables.

The lookup tables and multiple-node structures are used not only in the generalized HB retrievals, but also in simulating the measured reflectivity factors at Ka-band. Note that given the Ku-band normalized reflectivity value Z/N_0 and the lookup tables for both Ku- and Ka-band normalized reflectivity and attenuation, the associated Ka reflectivity and attenuation can be readily determined. The Ka-band measured reflectivity factors are simulated using (2). Attenuation due to cloud and water vapor is parameterized as described in Iguchi et al. (2009). The benefit of simulating measured Ka-band reflectivity from Ku-band precipitation profile estimates is that an objective procedure to optimally derive the N_0 values that make the Ku-band estimates most consistent with Ka-band observations can be derived. Such a procedure is described in the next subsection.

d. Optimal estimation framework

The agreement between simulated and actual measured Ka-band reflectivity factors could be assessed using the following cost function:

$$F_Z(\mathbf{N}_0) = \frac{1}{2} [\mathbf{Z}_{m,Ka} - \mathbf{Z}_{sim,Ka}(\mathbf{N}_0)]^T \mathbf{W}_Z^{-1} \times [\mathbf{Z}_{m,Ka} - \mathbf{Z}_{sim,Ka}(\mathbf{N}_0)], \quad (9)$$

where $\mathbf{Z}_{m,Ka}$ is the actual Ka-band measured reflectivity vector (dBZ), $\mathbf{Z}_{sim,Ka}(\mathbf{N}_0)$ is the Ka-band reflectivity vector simulated from Ku-band retrievals, and \mathbf{W}_Z is the reflectivity error covariance. The formulation in (9) is generally insufficient to derive well-defined estimates of N_0 (i.e., estimates that are unique and insensitive to small perturbations in the measurements), based on the agreement between simulated and actual measured Ka-band reflectivity factors. A more complete formulation that accounts for the agreement between simulated and SRT-derived PIAs and between estimated N_0 and a priori N_0 estimates is

$$F(\mathbf{N}_0) = F_Z(\mathbf{N}_0) + \frac{1}{2} [\mathbf{PIA}_{SRT} - \mathbf{PIA}_{sim}(\mathbf{N}_0)]^T \mathbf{W}_{PIA}^{-1} \times [\mathbf{PIA}_{SRT} - \mathbf{PIA}_{sim}(\mathbf{N}_0)] + \frac{1}{2} [\ln(\mathbf{N}_0^a) - \ln(\mathbf{N}_0)]^T \mathbf{W}_N^{-1} [\ln(\mathbf{N}_0^a) - \ln(\mathbf{N}_0)], \quad (10)$$

where \mathbf{PIA}_{SRT} is the two-component vector of SRT estimates of Ku- and Ka-band PIA, $\mathbf{PIA}_{sim}(\mathbf{N}_0)$ is the vector of Ku- and Ka-band PIA simulated from the Ku retrievals, \mathbf{W}_{PIA} is a matrix of associated uncertainties, $\ln(\mathbf{N}_0^a)$ is an a priori independent estimate of $\ln(\mathbf{N}_0)$, and \mathbf{W}_N is a matrix of associated uncertainties. In this study, \mathbf{W}_Z and \mathbf{W}_{PIA} are specified as in Grecu and Olson (2008).

Vector \mathbf{N}_0^a and matrix \mathbf{W}_N are derived from Weather Research and Forecasting Model (WRF, Skamarock et al. 2005) simulations of tropical convection using the WRF two-moment microphysical scheme (Morrison et al. 2005). Specifically, two 48-h-long simulations of convection that occurred during the period and in the region of the Tropical Composition, Cloud and Climate Coupling (TC4) Experiment (Toon et al. 2010) are produced and used to derive vector \mathbf{N}_0^a and matrix \mathbf{W}_N . Previous studies (e.g., Rao et al. 2001; Bringi et al. 2003; Rosenfeld and Ulbrich 2003; Steiner et al. 2004) indicate that particle size distributions vary considerably in time and space as a function of a multitude of factors such as aerosol load, surface type, synoptic conditions, and orographic forcing. It is therefore unlikely that the indiscriminate use of \mathbf{N}_0^a and matrix \mathbf{W}_N derived using simulations of a specific type of precipitation would produce globally optimal rain estimates. Therefore, additional simulations and estimates of \mathbf{N}_0^a and matrix \mathbf{W}_N are necessary for the algorithm to be optimal in different meteorological contexts.

Function F does not depend exclusively on N_0 but on other parameters as well (e.g., the shape factors, cloud water, and relative humidity). However, given that these parameters cannot be reliably retrieved along with N_0 from dual-frequency radar observations, they are specified rather than retrieved. Some information regarding the relative humidity and cloud water distribution can be derived from coincident microwave radiometer observations if available, but this study's focus is exclusively dual-frequency spaceborne radar retrievals. Combined radar–radiometer retrievals will be investigated in a future study, and so only the *sensitivity* of precipitation estimates to parameters that cannot be retrieved from radar observations alone will be considered here.

To derive a Ku-band retrieval that is physically consistent with both Ka-band radar observations and SRT PIA estimates, the functional F in (10) is minimized as a function of $\ln(\mathbf{N}_0)$ using the Gauss–Newton method (Rodgers 2000). Addressing the minimization problem as a function of $\ln(\mathbf{N}_0)$, rather than \mathbf{N}_0 , is advantageous because it requires the linearization of only the first two terms on the right-hand side of (10). The flowchart of the minimization procedure is shown in Fig. 2. The Gauss–Newton method requires the Jacobian of the forward model operator, that is, the operator that, given the vector \mathbf{N}_0 , produces the simulated observations $\mathbf{Z}_{sim,Ka}(\mathbf{N}_0)$ and $\mathbf{PIA}_{sim}(\mathbf{N}_0)$. In this study, the derivatives of the forward model operator's Jacobian, called \mathbf{H} here, are calculated using a finite-difference technique. That is, each component of the state vector \mathbf{N}_0 is varied independently of the other components, and the simulated observations are recalculated and then differenced with respect to the unperturbed simulated observations. The cost of

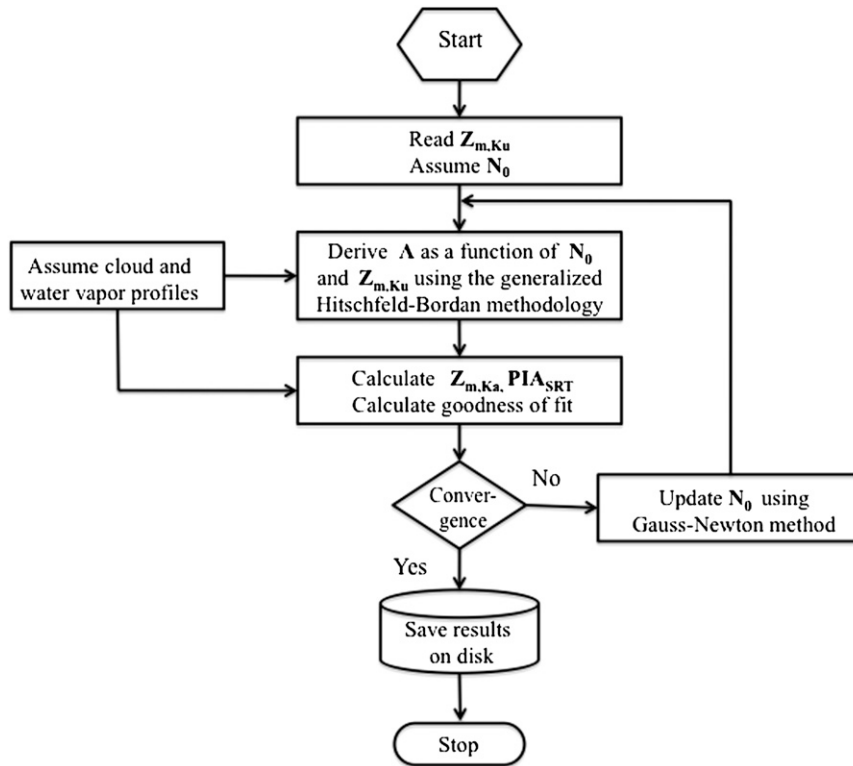


FIG. 2. Flowchart of the optimal estimation procedure.

calculating the Jacobian in this way is an order of magnitude higher than calculating the gradient of F through a reverse evaluation technique (Wunsch 2006). However, because the Gauss–Newton method is a second-order method, the minimization process requires a significantly smaller number of iterations than steepest descent techniques based on reverse gradient evaluations, which makes the Gauss–Newton method similar in terms of computational effort to the reverse-gradient-based techniques. The vector \mathbf{N}_0 is updated using the following formula:

$$\ln(\mathbf{N}_{0,k+1}) = \ln(\mathbf{N}_{0,k}) + \mathbf{A}^{-1}[\mathbf{A}^T \mathbf{R}^{-1} \mathbf{dY} + \mathbf{W}_{\mathbf{N}}^{-1}(\mathbf{N}_0^a - \mathbf{N}_0)], \quad (11)$$

where

$$\mathbf{R}^{-1} = \begin{bmatrix} \mathbf{W}_{\mathbf{Z}}^{-1} & 0 \\ 0 & \mathbf{W}_{\text{PIA}}^{-1} \end{bmatrix},$$

$\mathbf{A} = \mathbf{H}^T \mathbf{R}^{-1} \mathbf{H} + \mathbf{W}_{\mathbf{N}}^{-1}$, and \mathbf{dY} is the difference between the observations and simulations. Another advantage of the Gauss–Newton method is that \mathbf{A}^{-1} represents the error covariance of the $\ln(\mathbf{N}_0)$ estimates.

The whole process of deriving Λ as a function of \mathbf{N}_0 from the Ku-band observations, simulating the Ka-band

measurements and the PIA vector, and updating the \mathbf{N}_0 vector is illustrated in Fig. 2. For the purposes of computational efficiency as well as numerical robustness, it is preferable to retrieve a reduced-order representation of \mathbf{N}_0 rather than N_0 at every single radar gate where dual-frequency observations are available; see Hogan (2007). That is, N_0 is retrieved every 500 m, and the intermediate values are determined by spline interpolation of $\log(N_0)$. Although the resulting \mathbf{N}_0 is smoother than it would be if it were explicitly retrieved for every gate, the associated estimates of Λ and other variables are not necessarily smooth because independent Λ retrievals are carried out for every radar gate using the generalized HB method. It is worth mentioning that Rose and Chandrasekar (2006) also used a parameterized representation of $\log(N_0)$: they assumed that for liquid rain, $\log(N_0)$ varies linearly with height. However, unlike in the current approach, the mass-weighted mean diameter was also parameterized. In subsequent sections, the least squares–based algorithm described in this section will be referred to as LSA.

3. Application to synthetic data

To assess the LSA’s ability to yield a well-defined solution, a synthetic data experiment is devised. That is,

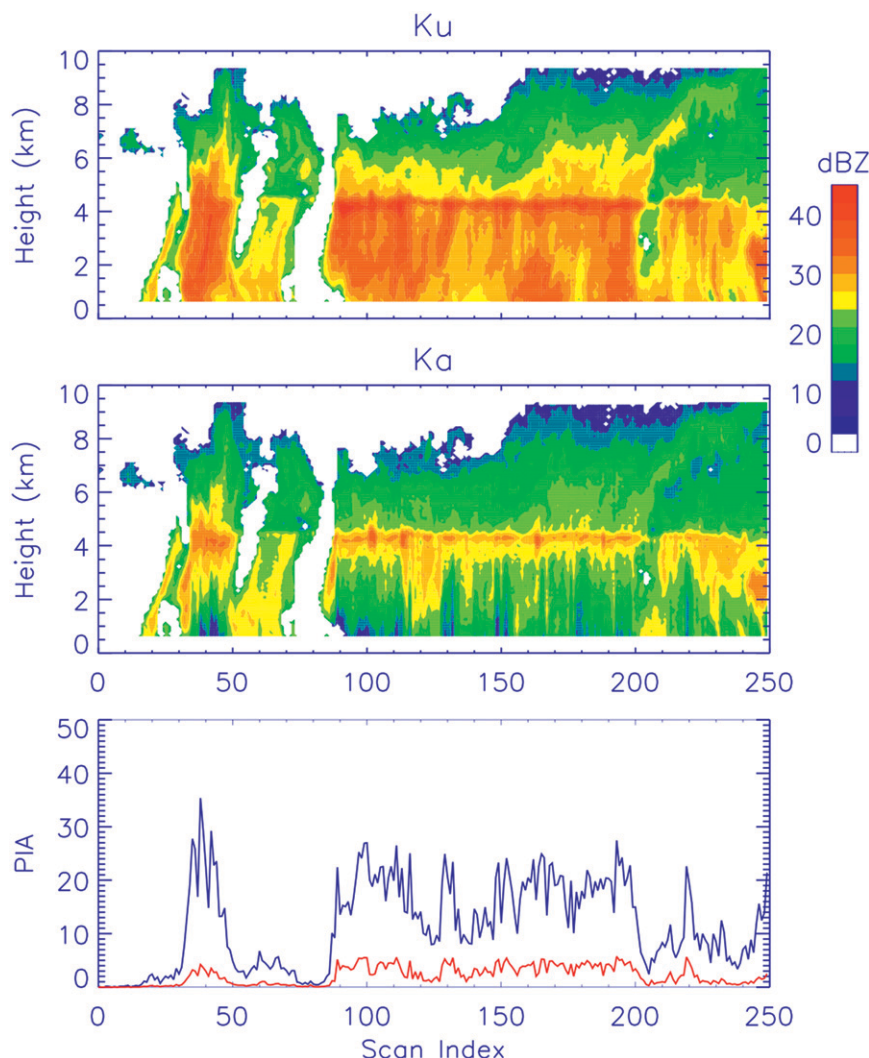


FIG. 3. Synthetic Ku- and Ka-band reflectivity observations.

the algorithm is applied to simulated dual-frequency Ku-/Ka-band observations, and the results are evaluated against the PSD variables used to simulate the observations. Actual Ku-band airborne radar observations collected in the TC4 experiment (Toon et al. 2010) are used to derive vertical profiles of slope profiles (Λ) as a function of randomly generated N_0 profiles. Uncorrelated, lognormally distributed N_0 values with a mean of $\log(0.08 \text{ cm}^{-4})$ and a standard deviation of 1.0 are generated every 500 m starting from the Ku-band echo top down to surface. The intermediate N_0 values are computed by spline interpolation, as explained in previous section. The shape factor μ is assumed constant in the vertical and equal to 0.0. Given the randomly generated N_0 profiles, fixed μ , and Ku-band reflectivity profile, a synthesized Λ profile is derived using the generalized HB method. The cloud water and relative

humidity profiles are assumed known and set based on the WRF simulations. These profiles are assumed to be representative of tropical precipitation. Finally, Ka-band reflectivities, as well as Ku- and Ka-band PIAs, are then synthesized from the known atmospheric profile and the forward model. Although the vertical distributions of cloud and relative humidity may have a significant impact on both Ku- and Ka-band retrievals, only the mechanics of the algorithm and not the impact of uncertainties in forward models are tested in this section.

Shown in Fig. 3 are the synthetic Ku-band and Ka-band reflectivity observations. Single-frequency (Ku only; left-hand panel) and dual-frequency (Ku/Ka; right-hand panel) estimates of precipitation water content are plotted versus the “true” precipitation water contents in Fig. 4. Data points from all levels are shown in the figure. It is apparent from Fig. 4 that the dual-frequency,

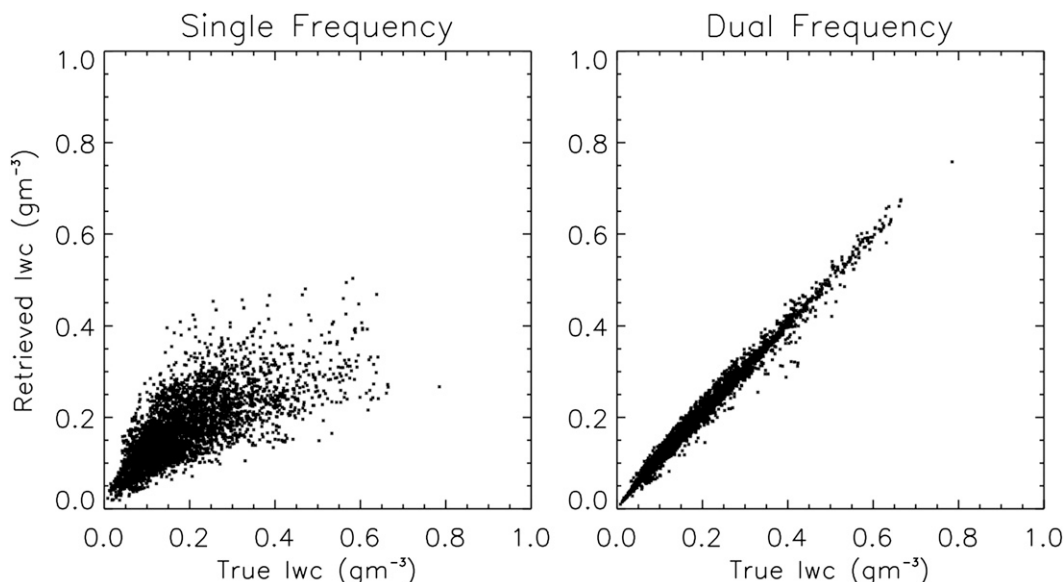


FIG. 4. True vs estimated equivalent precipitation water content derived from (left) single (Ku band) and (right) dual-frequency synthetic (Ku/Ka band) observations.

Ku-/Ka-band estimates are superior to single-frequency, Ku-band estimates, and that the LSA estimates are reasonably accurate. In applications to actual radar data, the vertical distributions of μ , cloud water, and relative humidity are not known, and any reasonable assumption may have a notable impact on retrievals. The electromagnetic properties of the melting layer represent a source of significant uncertainty as well. Therefore, the results described in this section should be regarded only

as an evaluation of the LSA's ability to provide a correct solution to the numerical problem associated with the retrieval process.

Shown in Fig. 5 are single-frequency (Ku band; left-hand panel) and dual-frequency (Ku/Ka band; right-hand panel) retrievals of mass-weighted mean diameters from the semisynthetic observations. Similar to the results in Fig. 4, the dual-frequency retrievals are superior to single-frequency retrievals. However, as previously

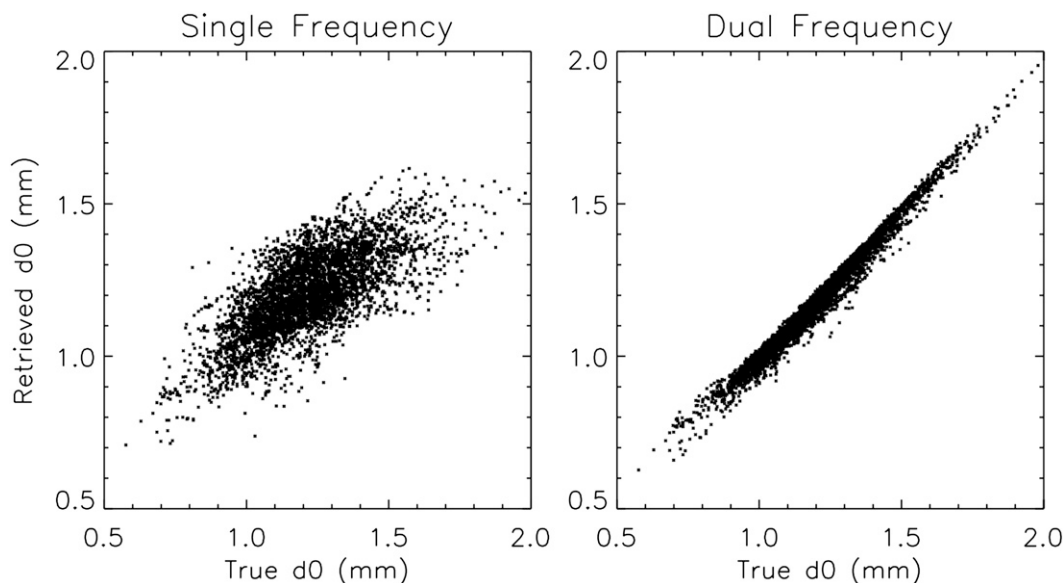


FIG. 5. True vs estimated equivalent mass-weighted mean diameters derived from (left) single (Ku band) and (right) dual-frequency synthetic (Ku/Ka band) observations.

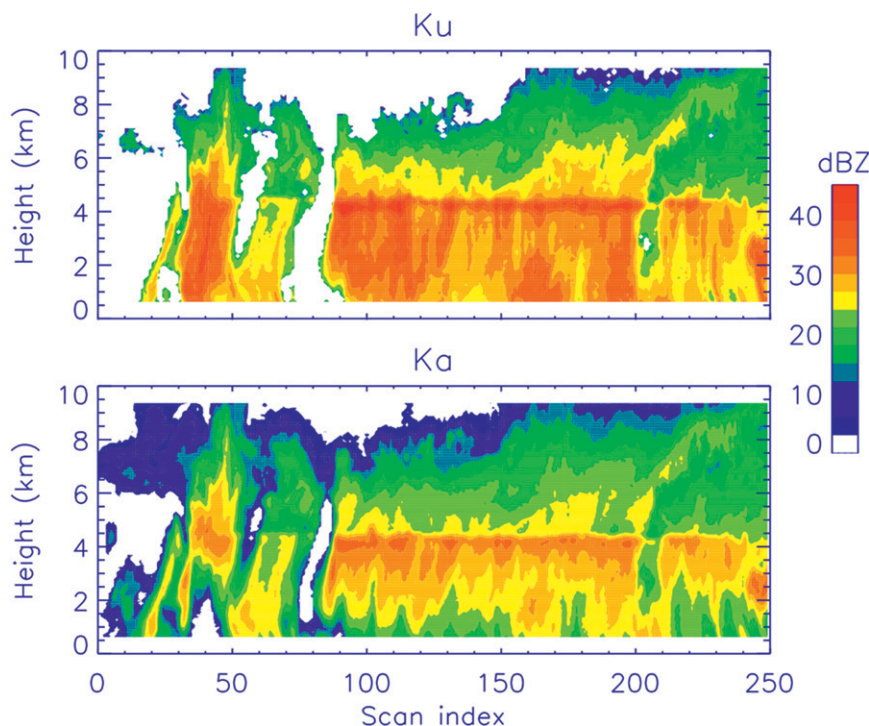


FIG. 6. Ku- and Ka-band reflectivity observations from the APR-2 at the TC4 field experiment on 17 Jul 2007.

explained, additional uncertainties are expected to arise in real-life applications.

4. Application to airborne data

In this section, the dual-frequency algorithm is applied to actual radar observations collected by the Airborne Second Generation Precipitation Radar (APR-2) during the TC4 experiment. TC4 was based in Costa Rica and Panama during July and August 2007. Its major objective was to better understand the role that the tropical tropospheric layer (TTL) plays in the earth's climate and atmospheric chemistry (Toon et al. 2010). APR-2 provides collocated beam reflectivity observations at 13.4 and 35.6 GHz in a downward-looking, cross-track-scanning geometry (Sadowy et al. 2003). Given its similarity to the future GPM DPR, APR-2 data represent an excellent opportunity to test DPR algorithms. The real Ku-/Ka-band data used in this section were collected during a flight leg that occurred from 1936 to 1944 UTC 17 July 2007. During this flight leg, the APR-2 sampled both convective (apparent near scan index 40 in Fig. 6) and stratiform precipitation. The dual-frequency retrievals are expected to be more accurate in stratiform precipitation, since the vertical distribution of precipitation phases are better defined in stratiform regions.

However, the algorithm developed here is applicable to both convective and stratiform precipitation.

Shown in Fig. 7 are the equivalent mass-weighted mean diameter (top panel) and the equivalent precipitation water content (middle panel) derived by the application of the LSA to the observations shown in Fig. 6. The shape factor μ is assumed to be 0.0 in this algorithm application. Generic relative humidity and cloud profiles derived from WRF simulations are assumed, as explained in the previous section. A snow density of 0.1 g cm^{-3} is also assumed. The impact of these assumptions on the retrieved precipitation will be investigated later in this section.

Although some artifacts are apparent, the precipitation estimates appear to be realistic. The reason why the mass-weighted mean diameter tends to be larger in the melting layer than in the immediate neighboring layers is most likely an underestimation of the dual-frequency reflectivity ratio (DFR) in the melting layer due to the relatively simple model of electromagnetic properties of melting ice particles. It should be noted here that not only the model of Klaassen (1988) is deficient in this respect. Several other simple models of similar design (i.e., based on the assumption that melting particles are spherical mixtures of air, ice, and liquid water) have been explored and did not produce better results. Although

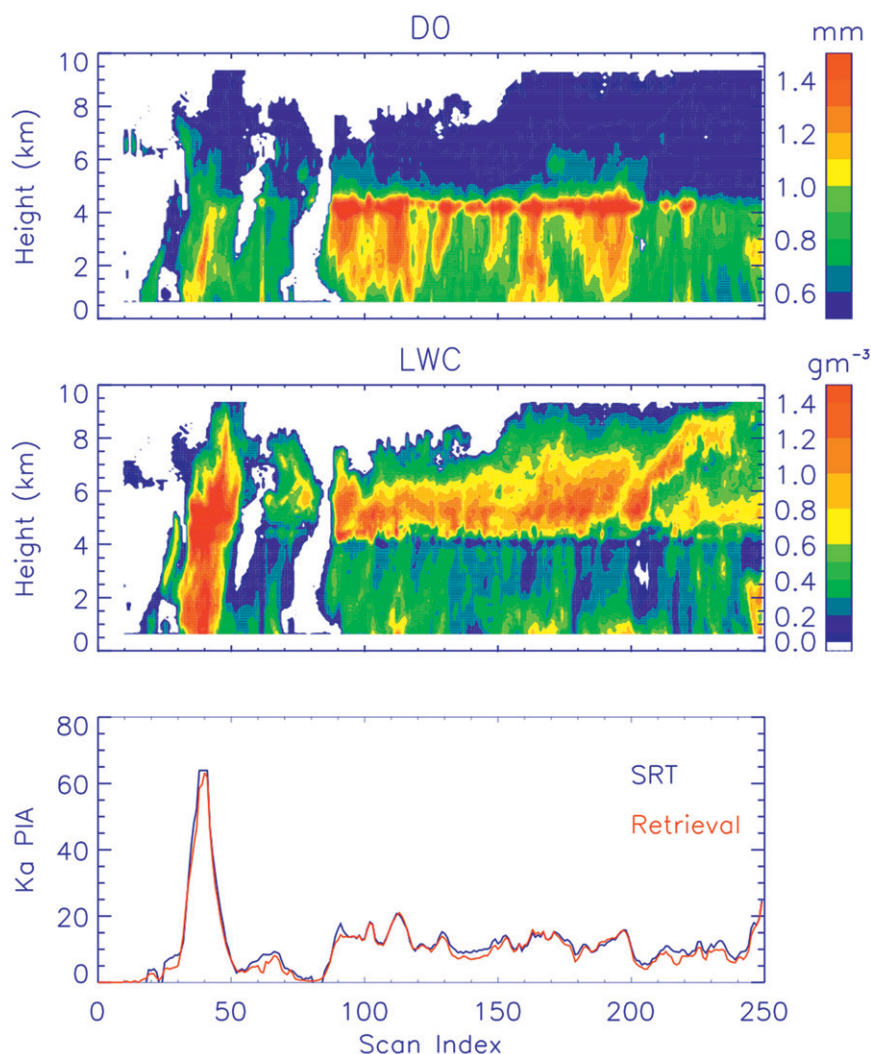


FIG. 7. (top) Equivalent mass-weighted mean diameters, (middle) equivalent precipitation water contents, and (bottom) PIAs estimated from the APR-2 data between 1936 and 1944 UTC 17 Jul 2007.

the more complex approach of Liao and Meneghini (2005) is likely to yield a more continuous transition from the ice to the liquid water phase, tables of electromagnetic scattering properties (e.g., extinction, scattering, phase function) at all GPM frequencies are not yet available. However, such tables will become available in the near future (L. Liao and R. Meneghini 2010, personal communications), and they will be incorporated into the LSA. Until then, the electromagnetic model of Klaassen (1988) will be used. The consequence of DFR underestimation in the bright band is the underestimation of N_0 in the bright band. Therefore, the Ku-band reflectivity in the bright band is interpreted as being caused by unrealistically few but relatively large particles, leading to an underestimation of precipitation water contents in the bright band.

Shown in the bottom panel of Fig. 7 are the Ka-band SRT PIA and the algorithm-estimated PIA. There is good agreement between the two variables, which indicates that the precipitation estimates are consistent with Ka-band reflectivity observations as well as the SRT PIA at Ka band. The agreement is good even in the convective region, which is characterized by very large Ka-band PIA—an illustration of the algorithm's ability to make use of all existing information. That is to say, even though the Ka-band reflectivity signal can become completely attenuated (see Fig. 6), the SRT PIA estimate may still provide useful information to the algorithm. Note that formulations that make explicit use of the dual-frequency reflectivity ratio cannot use this type of information in the retrieval process. The Ku-band SRT and retrieved PIAs exhibit similar agreement (not shown).

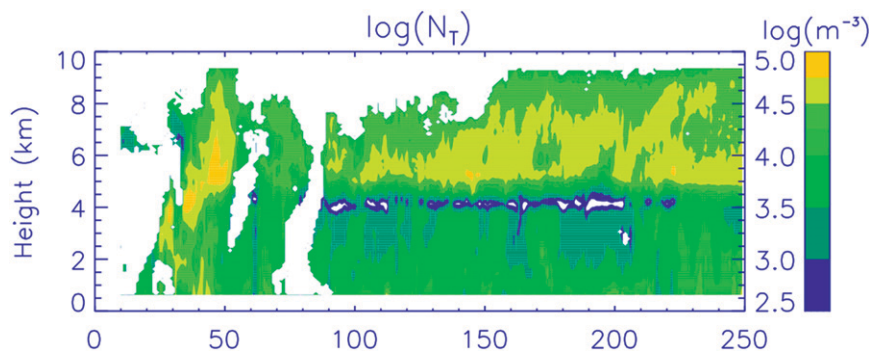


FIG. 8. Estimated N_T values from the APR-2 between 1936 and 1944 UTC 17 Jul 2007.

The retrieved number density N_T , defined as the total number of precipitation particles per volume unit, is shown in Fig. 8. A trend of increasing N_T with the distance below the cloud top is apparent above 5-km altitude. Lo and Passarelli (1982) noted a similar trend in airborne data and attributed it to depositional growth of ice nuclei. In the freezing regions close to the 0°C isotherm, a decrease of N_T with the distance from cloud top is expected because of aggregation processes. Uncertainties in modeling the electromagnetic scattering properties and size distributions of ice-phase precipitation are likely to significantly affect the N_T retrieval in the ice phase. Although progress in modeling the scattering properties using advanced electromagnetic solvers and complex particle shapes (Liu 2008) and better parameterizations of snow distributions (Tian et al. 2010) are likely to reduce uncertainties in the ice-phase estimates of N_T , it is expected that ice-phase retrievals will continue to be more uncertain than liquid-phase retrievals simply because of the additional degrees of freedom involved in the characterization of frozen hydrometeors versus raindrops. Similarly, N_T estimates in the melting layer are likely to have significant uncertainties due to uncertainties in both electromagnetic properties and particle size distribution parameterizations. Estimates of N_T near the ground in clutter-free regions are expected to be most accurate when the SRT estimates of PIA are accurate. This is because, irrespective of forward modeling uncertainties, the algorithm derives a solution that is consistent with Ku- and Ka-band reflectivity observations as well as the associated SRT PIAs. Therefore if the SRT PIAs are reasonably accurate, then precipitation estimates from LSA will be similar to those of Meneghini et al. (1992), which are deemed most accurate near the ground. In sum, the LSA does not require SRT estimates of PIAs, but it does make effective use of them if they are available and accurate.

To investigate the impact of the SRT PIA estimates, retrievals without the use of these estimates are performed.

This is done by setting the elements of \mathbf{W}_{PIA} to very large values, which makes the contribution of the second term on the right-hand side of (10) essentially zero irrespective of the model-derived PIAs. The differences between the reference precipitation estimates and the estimates derived without PIA information are shown in the top panel of Fig. 9. Note that the differences are negligible at and above the freezing level, but they increase close to the ground, where the ratios of attenuation-corrected reflectivity factors to attenuated reflectivity factors should be approximately equal to the SRT PIAs. This is an indication that SRT PIA estimates may have a significant impact on retrievals of near-surface precipitation and that estimates derived exclusively from reflectivity observations may not be necessarily consistent with the SRT estimates of PIA.

The differences between the SRT-based LSA estimates and single-frequency (Ku only) estimates are shown in the bottom panel of Fig. 9. The differences between the two retrievals are significant both above and below the freezing level. Nevertheless, it is still possible to make the single-frequency radar precipitation estimates more consistent with dual-frequency radar estimates. In the LSA applications shown in Fig. 9, the a priori $\ln(\mathbf{N}_0^a)$ estimate and its associated covariance matrix (derived here from WRF simulations) are not consistent with the \mathbf{N}_0 estimates derived from the dual-frequency observations. However, in satellite applications, more representative estimates of $\ln(\mathbf{N}_0^a)$ and \mathbf{W}_N for single-frequency applications can be derived from the long-term application of the LSA to dual-frequency observations. The use of such a priori estimates is likely to produce single-frequency (Ku only) retrievals that are more consistent with the dual-frequency retrievals than those utilizing WRF estimates of $\ln(\mathbf{N}_0^a)$ and \mathbf{W}_N . It should be mentioned that in light rain, a Ka-band signal above the noise threshold may occur while the Ku-band signal is below the noise threshold. For such situations, a single-frequency Ka-band retrieval algorithm may be

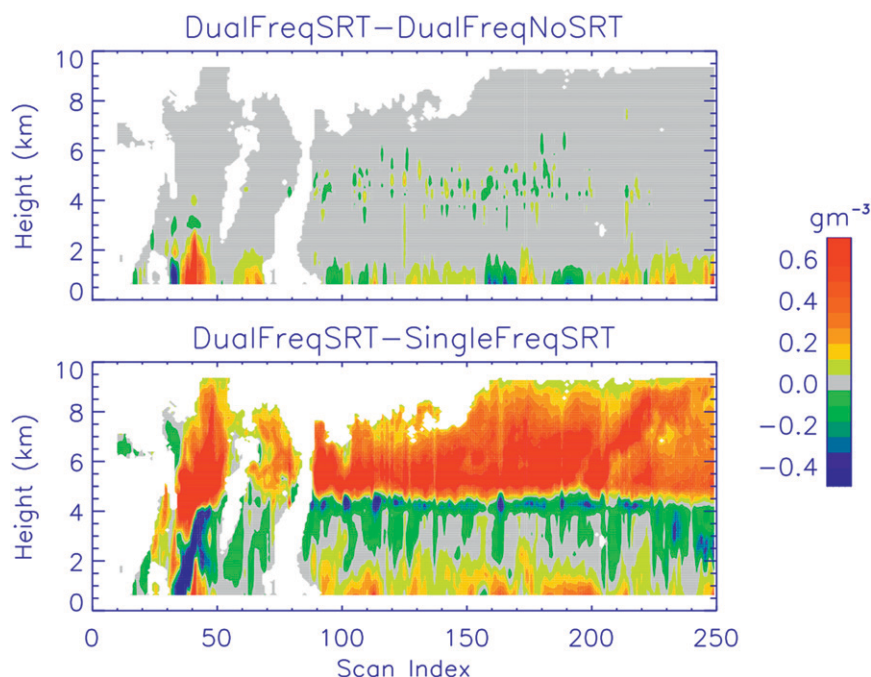


FIG. 9. (top) Differences of precipitation water contents estimated using LSA with and without SRT information and (bottom) differences estimated using LSA with dual-frequency (Ku/Ka band) and single-frequency (Ku band) data.

developed using the $\ln(N_0^a)$ and W_N information derived from the dual-frequency retrievals. It should be mentioned that the $\ln(N_0^a)$ and W_N information derived from dual-frequency observations may not be representative of light rain in situations in which only Ka band is above the noise threshold. However, better information may be difficult to derive and, until such information becomes available, the dual-frequency retrievals can provide a temporary solution.

To evaluate the sensitivity of precipitation estimates to parameters that cannot be reliably estimated from radar observations alone, retrievals under various assumptions are performed. Shown in the top panel of Fig. 10 is the difference between the LSA retrieval for $\mu = 0$ and the LSA retrieval for $\mu = 1$. As illustrated by Fig. 10, the PSD shape factor has a significant impact on precipitation water content estimates; the estimates for $\mu = 0$ being approximately 15% larger than those for $\mu = 1$. Cloud and relative humidity uncertainties may also result in uncertainties up to 10% in estimated water contents (results not shown). It is anticipated that these uncertainties can be reduced by incorporating LSA into a combined radar–radiometer framework, but the performance of such an algorithm will be the subject of a separate study, and so the investigation of combined radar–radiometer retrievals is deferred. Finally, the differences between LSA estimates derived using

two different snow densities, namely 0.10 g m^{-3} and 0.15 g m^{-3} , are displayed in the bottom panel of Fig. 7. As discussed previously, retrievals above the freezing level are highly sensitive to assumed snow particle electromagnetic scattering properties, which depend on the snow density. The use of high-frequency radiometer observations may reduce the uncertainties in snow water content estimates if more complex scattering calculations (e.g., Liu 2008) based on realistic snow habits (e.g., Westbrook et al. 2004) are employed.

5. Conclusions

In this study, an algorithm to retrieve precipitation vertical profiles from spaceborne dual-frequency (Ku/Ka band) radar observations is formulated and investigated. The algorithm is based on a generalized HB attenuation correction methodology that yields generic PSD profiles from Ku-band radar data and an optimization procedure that adjusts the Ku-band-derived PSDs to make them more consistent with coincident Ka-band reflectivity observations and SRT PIA estimates at both Ku and Ka bands. The consistency between the Ku-band retrievals, the Ka-band reflectivity observations, and SRT PIA estimates at both Ku and Ka bands is quantified using a quadratic cost function that is minimized with respect to parameterized profiles of PSD intercepts using a Gauss–Newton method.

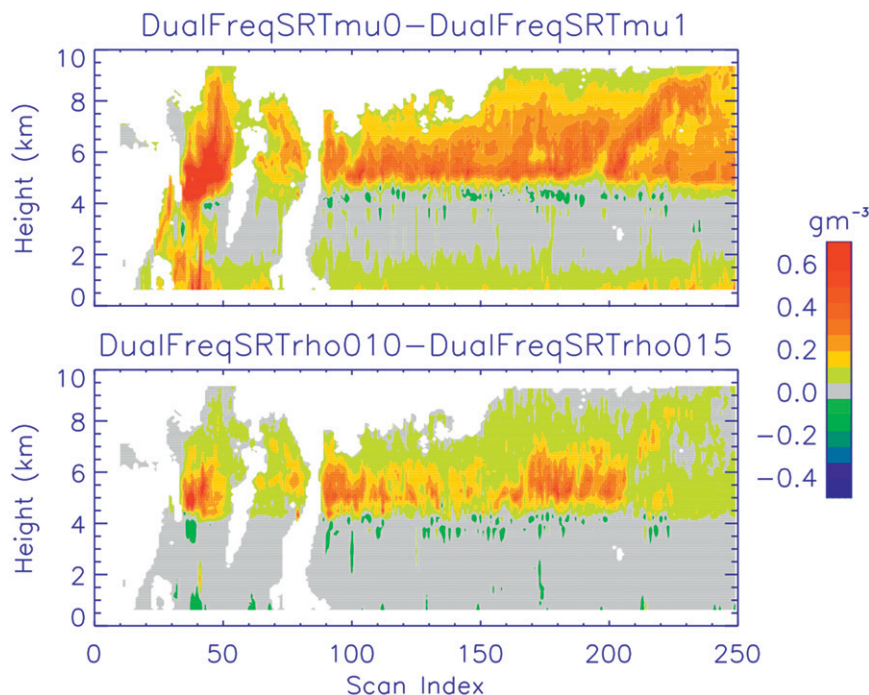


FIG. 10. Differences of estimated precipitation water contents using LSA, assuming different (top) shape factors and (bottom) snow densities. The assumed shape factors in the top panel are $\mu = 0.0$ and $\mu = 1.0$, while the assumed snow densities in the bottom panel are 0.1 and 0.15 g m^{-3} .

The algorithm is tested using both synthetic and actual airborne data. In the synthetic data evaluation, actual Ku-band radar observations along with assumed profiles of PSD intercepts, cloud water, and relative humidity are used to generate Ka-band observations. Retrievals using the synthetic data show the algorithm's ability to estimate two-parameter PSD information from dual-frequency observations. Alternatively, if only Ku-band data are available, the same algorithm yields estimates of PSDs with reasonable, but greater, levels of uncertainty.

The algorithm is applied to actual airborne observations from the TC4 field experiment with and without SRT PIA incorporated into the retrieval process. The SRT PIA information is found to have a significant impact on precipitation estimates, especially near the earth's surface, which is an indication that dual-frequency above-ground reflectivity observations alone may be insufficient for deriving unbiased precipitation estimates, and that SRT PIA information, when reliable, should be utilized in the retrieval process. Retrieved precipitation is also shown to be sensitive to the assumed shape of the particle size distribution, the assumed cloud water and water vapor distributions, and the assumed snow density. The inclusion of the dual-frequency algorithm within a combined radar-radiometer retrieval framework is expected to reduce the sensitivity of precipitation estimates to these factors. Also, valuable insight should be gained

from the analysis of dual-frequency radar and in situ observations originating from future field campaigns.

Future work needs to be carried out to assess this algorithm's performance and robustness within a combined radar-radiometer retrieval framework. Given the sensitivity of radiometer observations to variables that cannot be estimated from radar observations alone (e.g., cloud water, water vapor, snow density) combined radar-radiometer retrievals are likely to be better conditioned and consequently less uncertain than radar-only retrievals. However, because the physical modeling of both radar reflectivities and radiometer-sensitive microwave radiances is subject to uncertainties, the effort to develop combined radar-radiometer retrieval methods should be coupled with rigorous studies to accurately assess the uncertainties in radar and radiometer forward modeling.

Acknowledgments. This research was supported by NASA's Precipitation Measurement Missions (PMM) program. The contribution by Dr. Simone Tanelli was performed at the Jet Propulsion Laboratory, California Institute of Technology under contract with the National Aeronautics and Space Administration. The manuscript benefited from the constructive comments of three anonymous reviewers.

REFERENCES

- Bauer, P., A. Khain, A. Pokrovsky, R. Meneghini, C. Kummerow, F. Marzano, and J. P. V. Poiares Baptista, 2000: Combined cloud-microwave radiative transfer modeling of stratiform rainfall. *J. Atmos. Sci.*, **57**, 1082–1104.
- Bringi, V. N., V. Chandrasekar, J. Hubbert, E. Gorgucci, W. L. Randeu, and M. Schoenhuber, 2003: Raindrop size distribution in different climatic regimes from disdrometer and dual-polarized radar analysis. *J. Atmos. Sci.*, **60**, 354–365.
- Durden, S. L., and Z. S. Haddad, 1998: Comparison of radar rainfall retrieval algorithms in convective rain during TOGA COARE. *J. Atmos. Oceanic Technol.*, **15**, 1091–1096.
- Ferreira, F., P. Amayenc, S. Oury, and J. Testud, 2001: Study and tests of improved rain estimates from the TRMM precipitation radar. *J. Appl. Meteor.*, **40**, 1878–1899.
- Greco, M., and E. N. Anagnostou, 2004: A differential attenuation based algorithm for estimating precipitation from dual-wavelength spaceborne radar observations. *Can. J. Remote Sens.*, **30**, 697–705.
- , and W. S. Olson, 2008: Precipitating snow retrievals from combined airborne cloud radar and millimeter wave radiometer observations. *J. Appl. Meteor. Climatol.*, **47**, 1634–1650.
- , —, and E. N. Anagnostou, 2004: Retrieval of precipitation profiles from multiresolution, multifrequency, active and passive microwave observations. *J. Appl. Meteor.*, **43**, 562–575.
- Haddad, Z. S., E. A. Smith, C. D. Kummerow, T. Iguchi, M. R. Farrar, S. L. Durden, M. Alves, and W. S. Olson, 1997: The TRMM “day-1” radar/radiometer combined rain-profiling algorithm. *J. Meteor. Soc. Japan*, **75**, 799–809.
- Hitschfeld, W., and J. Bordan, 1954: Errors inherent in the radar measurement of rainfall at attenuating wavelengths. *J. Meteor.*, **11**, 58–67.
- Hogan, R. J., 2007: A variational scheme for retrieving rainfall rate and hail reflectivity fraction from polarization radar. *J. Appl. Meteor. Climatol.*, **46**, 1544–1564.
- Hou, A. Y., G. Skofronick-Jackson, C. D. Kummerow, and J. M. Shepherd, 2008: Global precipitation measurement. *Precipitation: Advances in Measurement, Estimation and Prediction*, S. C. Michaelides, Ed., Springer, 131–170.
- Iguchi, T., and R. Meneghini, 1994: Intercomparison of single-frequency methods for retrieving a vertical rain profile from airborne or spaceborne radar. *J. Atmos. Oceanic Technol.*, **11**, 1507–1516.
- , T. Kozu, J. Kwiatkowski, R. Meneghini, J. Awaka, and K. Okamoto, 2009: Uncertainties in the rain profiling algorithm for the TRMM precipitation radar. *J. Meteor. Soc. Japan*, **87**, 1–30.
- Illingworth, A. J., and T. M. Blackman, 2002: The need to represent raindrop size spectra as normalized gamma distributions for the interpretation of polarization radar observations. *J. Appl. Meteor.*, **41**, 286–297.
- Klaassen, W., 1988: Radar observations and simulation of the melting layer of precipitation. *J. Atmos. Sci.*, **45**, 3741–3753.
- Liao, L., and R. Meneghini, 2005: On modeling air/spaceborne radar returns in the melting layer. *IEEE Trans. Geosci. Remote Sens.*, **43**, 2799–2809.
- , —, T. Iguchi, and A. Detwiler, 2005: Use of dual-wavelength radar for snow parameter estimates. *J. Atmos. Oceanic Technol.*, **22**, 1494–1506.
- Liu, G., 2008: A database of microwave single-scattering properties for nonspherical ice particles. *Bull. Amer. Meteor. Soc.*, **89**, 1563–1570.
- Lo, K. K., and R. E. Passarelli, 1982: The growth of snow in winter storms: An airborne observational study. *J. Atmos. Sci.*, **39**, 697–706.
- Mardiana, R., T. Iguchi, and N. Takahashi, 2004: A dual-frequency rain profiling method without the use of a surface reference technique. *IEEE Trans. Geosci. Remote Sens.*, **42**, 2214–2225.
- Masunaga, H., and C. D. Kummerow, 2005: Combined radar and radiometer analysis of precipitation profiles for a parametric retrieval algorithm. *J. Atmos. Oceanic Technol.*, **22**, 909–929.
- Maxwell-Garnett, J. C., 1904: Colors in metal glasses and in metallic films. *Philos. Trans. Roy. Soc. London*, **203A**, 385–420.
- Meneghini, R., 1978: Rain-rate estimates for an attenuating radar. *Radio Sci.*, **13**, 459–470.
- , T. Kozu, H. Kumagai, and W. Boncyk, 1992: A study of rain estimation methods from space using dual-wavelength radar measurements at near-nadir incidence over ocean. *J. Atmos. Oceanic Technol.*, **9**, 364–382.
- , T. Iguchi, T. Kozu, L. Liao, K. Okamoto, J. A. Jones, and J. Kwiatkowski, 2000: Use of the surface reference technique for path attenuation estimates from the TRMM precipitation radar. *J. Appl. Meteor.*, **39**, 2053–2070.
- , J. A. Jones, T. Iguchi, K. Okamoto, and J. Kwiatkowski, 2004: A hybrid surface reference technique and its application to the TRMM precipitation radar. *J. Atmos. Oceanic Technol.*, **21**, 1645–1658.
- Morrison, H., J. A. Curry, and V. I. Khvorostyanov, 2005: A new double moment microphysics parameterization for application in cloud and climate models. Part I: Description. *J. Atmos. Sci.*, **62**, 1665–1677.
- Press, W. H., B. P. Flannery, S. A. Teukolsky, and W. T. Vetterling, 2007: *Numerical Recipes in FORTRAN: The Art of Scientific Computing*. 3rd ed. Cambridge University Press, 1256 pp.
- Rao, T. N., D. N. Rao, K. Mohan, and S. Raghavan, 2001: Classification of tropical precipitating systems and associated Z-R relationships. *J. Geophys. Res.*, **106** (D16), 17 699–17 711.
- Rodgers, C. D., 2000: *Inverse Methods for Atmospheric Sounding: Theory and Practice*. World Scientific, 238 pp.
- Rose, C. R., and V. Chandrasekar, 2006: A GPM dual-frequency retrieval algorithm: DSD profile-optimization method. *J. Atmos. Oceanic Technol.*, **23**, 1372–1383.
- Rosenfeld, D., and C. W. Ulbrich, 2003: Cloud microphysical properties, processes, and rainfall estimation opportunities. *Radar and Atmospheric Science: A Collection of Essays in Honor of David Atlas, Meteor. Monogr.*, No. 52, Amer. Meteor. Soc., 237–258.
- Sadowy, G. A., A. C. Berkun, W. Chun, E. Im, and S. L. Durden, 2003: Development of an advanced airborne precipitation radar. *Microwave J.*, **46**, 84–98.
- Senbokuya, Y., S. Satoh, K. Furukawa, M. Kojima, H. Hanado, N. Takahashi, T. Iguchi, and K. Nakamura, 2004: Development of the spaceborne dual-frequency precipitation radar for the Global Precipitation Measurement mission. *Proc. IGARSS 2004*, Anchorage, AK, IEEE, 3566–3569.
- Skamarock, W. C., J. B. Klemp, J. Dudhia, D. O. Gill, D. M. Barker, W. Wang, and J. G. Powers, 2005: A description of the Advanced Research WRF version 2. NCAR Tech. Note NCAR/TN-468+STR, 88 pp.
- Steiner, M., J. A. Smith, and R. Uijlenhoet, 2004: A microphysical interpretation of radar reflectivity–rain rate relationships. *J. Atmos. Sci.*, **61**, 1114–1131.

- Testud, J., S. Oury, P. Amayenc, and R. A. Black, 2001: The concept of “normalized” distributions to describe raindrop spectra: A tool for cloud physics and cloud remote sensing. *J. Appl. Meteor.*, **40**, 1118–1140.
- Tian, L., G. M. Heymsfield, L. Li, A. J. Heymsfield, A. Bansemer, C. H. Twohy, and R. C. Srivastava, 2010: A study of cirrus ice particle size distribution using TC4 observations. *J. Atmos. Sci.*, **67**, 195–216.
- Toon, O. B., and Coauthors, 2010: Planning, implementation, and first results of the Tropical Composition, Cloud and Climate Coupling Experiment (TC4). *J. Geophys. Res.*, **115**, D00J04, doi:10.1029/2009JD013073.
- Ulbrich, C. W., 1983: Natural variations in the analytical form of the raindrop size distribution. *J. Climate Appl. Meteor.*, **22**, 1764–1775.
- Westbrook, C. D., R. C. Ball, P. R. Field, and A. J. Heymsfield, 2004: Universality in snowflake aggregation. *Geophys. Res. Lett.*, **31**, L15104, doi:10.1029/2004GL020363.
- Wunsch, C., 2006: *Discrete Inverse and State Estimation Problems: With Geophysical Fluid Applications*. Cambridge University Press, 384 pp.